Eur. Phys. J. B (2019) 92: 111
https://doi.org/10.1140/epjb/e2019-100017-8

THE EUROPEAN PHYSICAL JOURNAL B

Regular Article

Variational Monte-Carlo study of the extended Bose-Hubbard model with short- and infinite-range interactions

Benjamin Bogner[1,a], Clément De Daniloff[2], and Heiko Rieger[1]

[1] Theoretical Physics, Saarland University, Campus E2.6, 66123 Saarbrücken, Germany
[2] École Normale Supérieure, 24 rue Lhomond, 75005 Paris, France

Received 11 January 2019 / Received in final form 21 March 2019
Published online 22 May 2019

Abstract. In this paper, we study the two-dimensional Bose-Hubbard model with short- and long-range interactions in the canonical ensemble. Using a Variational Monte-Carlo method, we obtain the phase diagrams containing four different phases: Mott insulator, density wave, superfluid and supersolid. The transition lines are determined using the structure factor and the superfluid density. We observe that the phase diagrams for short and long-range interactions are very similar quantitatively and qualitatively, but show also some significant differences. To evaluate the quality of our Variational approach, we compare our results with results published by other groups, obtained with various methods, such as an exact quantum Monte-Carlo algorithm and Gutzwiller Ansatz.

1 Introduction

The Bose-Hubbard model (BHM) has been a research focus since its introduction [1]. In its simplest version, restricted to nearest-neighbor boson-tunneling and on-site repulsion, the phase diagram comprises superfluid (SF) and Mott insulator (MI) phases. Quantum critical phenomena were investigated using increasingly elaborate quantum Monte-Carlo (QMC) methods and scaling analysis, exact diagonalization and renormalization group theory [2]. Especially the early works based on QMC [3,4], path-integral Monte-Carlo [5–7] and modern worm algorithms [8–12] have to be emphasized. These advanced techniques and their derivatives like the stochastic Green-function algorithm [13,14] gave further insight into the standard BHM in higher dimensions [15–20]. Approximative methods like mean-field theory [1], density-matrix renormalization group [21], Gutzwiller wave function optimization [22] or strong coupling expansion [23] were also applied to the BHM in its standard form [22,23] and to extended models [24–27].

The interest in models with nearest-neighbor, next-nearest-neighbor, dipolar or long-range interactions between bosons increased when experiments on boson-like systems, e.g. ultracold atoms trapped in optical lattices [28–31], became more elaborate and off-site interactions between particles [32] were implemented. In comparison to the standard BHM, these extended models exhibit richer phase diagrams with additional density wave (DW) and supersolid phases (SS) [33,34], which both feature long-range spatial ordering. In recent years, theoretical work explored the extended BHM with QMC methods [35–38], DMRG [39,40] and Gutzwiller Ansatz [41] for systems in and out of equilibrium.

Recently, an impactful experiment realized global-range interactions [42] between particles and ignited interest in its underlying Hamiltonian. To induce such long-range interactions between boson-like particles experimentally, ultracold atoms are placed inside of an optical cavity, which is able to propagate the interactions between the atoms. In this case, the particles interact via scattered photons. Standing waves inside the cavity emerge, resulting in long-range interactions between the atoms. Ground state phase diagrams of the corresponding model were compiled with the help of mean-field approaches in 1D [43], 2D [44–46] and 3D [47], with Gutzwiller ansatz [48,49], DMRG [39] and QMC methods [46,49,50]. Also, the dynamics of the model was investigated using dynamical mean-field methods [51] and quench dynamics for the hard-core Boson limit [52,53].

In this paper, we investigate Bose-Hubbard models with short-range and long-range interactions with the Variational Monte-Carlo method (VMC). This is an iterative method of wave-function optimization, based on Monte-Carlo simulations. Although it is rarely used to treat bosonic systems, this method has already delivered very good results for the standard BHM [54]. It has been shown that the method is appropriate for examining systems with long-range interactions [55]. We present the ground state phase diagrams of the different models at

[a] e-mail: bbogner@lusi.uni-sb.de

various densities and compare them under qualitative and quantitative aspects.

2 Models

We consider spinless bosons on a two-dimensional square lattice with periodic boundary conditions. Bosons can change their location by hopping to a neighboring site and interact repulsively with each other when occupying the same position. L denotes the edge length of the lattice, thus the number of sites is L^2. For reasons of symmetry, L is always chosen to be even. Note that all results were acquired within the canonical ensemble, i.e. for fixed particle number, which is specified by the VMC method. As stated in the introduction, we study the BHM with short-range interactions and with infinite-range interactions. The complete Hamiltonian with all interactions is given by

$$\hat{\mathcal{H}} = -t \sum_{\langle \mathbf{r},\mathbf{r}' \rangle} \left(\hat{b}^\dagger_{\mathbf{r}} \hat{b}_{\mathbf{r}'} + \hat{b}^\dagger_{\mathbf{r}'} \hat{b}_{\mathbf{r}} \right) + \frac{U_s}{2} \sum_{\mathbf{r}} \hat{n}_{\mathbf{r}} (\hat{n}_{\mathbf{r}} - 1) - \frac{U_l}{L^2} \left(\sum_{\mathbf{r} \in e} \hat{n}_{\mathbf{r}} - \sum_{\mathbf{r} \in o} \hat{n}_{\mathbf{r}} \right)^2 + U_{nn} \sum_{\langle \mathbf{r},\mathbf{r}' \rangle} \hat{n}_{\mathbf{r}} \hat{n}_{\mathbf{r}'} \quad (1)$$

where $\langle \cdots \rangle$ indicates the summation over all nearest-neighbors pairs on the lattice and the summations $\mathbf{r} \in e$, $\mathbf{r} \in o$ extend over even and odd lattice-sites respectively. The operators $\hat{b}_{\mathbf{r}}$ and $\hat{b}^\dagger_{\mathbf{r}}$ annihilate or create a boson at site $\mathbf{r}$, while $\hat{n}_{\mathbf{r}} = \hat{b}^\dagger_{\mathbf{r}} \hat{b}_{\mathbf{r}}$ is the number operator for site $\mathbf{r}$. The kinetic energy contribution is proportional to the hopping strength $t > 0$, $U_s > 0$ is the strength of the local on-site repulsive interaction. The nearest neighbor-interaction is tuned by U_{nn}, the long-range interaction by U_l.

2.1 Nearest-neighbor interactions

The first model we consider is an extended BHM featuring repulsive interactions between bosons on nearest-neighboring (NN) sites but no long-range interactions ($U_l = 0$). Aside from the kinetic energy term, which favors movement of bosons on the lattice and thereby delocalization, there is competition between the two short-ranged interactions in this Hamiltonian. The on-site repulsion promotes a uniform distribution of the particles on the lattice, in order to minimize the average deviation of the number of particles per site from the density. The NN repulsion, on the other hand, stimulates an imbalance in the occupation of adjacent sites, as multiple particles on the same site are energetically favored over particles on neighboring locations. While theoretical works in 2D [33,56] and 3D [57,58] discovered the resulting density wave and supersolid phases, early publications on 1D models were not able to confirm the existence of the supersolid phase for this dimension [24,25] yet. However, following approaches, which used Gutzwiller ansatz [59] and QMC [36], indicated the existence of a supersolid region in the ground state phase diagram of the 1D model. Since then, the BHM with NN interactions is a common subject to further investigation [19,26,35,60].

2.2 Long-range interactions

In the extended BHM with long-range (LR) interactions, the strength of off-site interactions is scaled by $U_l > 0$ ($U_{nn} = 0$). Drawing a comparison to the former case, the short-range interactions stimulate the formation of local imbalances, ultimately resulting in the development of a global pattern of imbalance. The LR interactions, however, promote imbalance on a global scale, because all particles on the lattice interact with each other and the strength of this interaction does not depend on their distance. An experimental realization of such a model was proposed [61,62], early simulations for the 1D and 2D system were done [50] and the existence of a supersolid phase was proposed [44].

Interest in this model was amplified when an experiment with cavity-induced LR interactions had been conducted [42]. Various methods delivered phase diagrams in 1D [43,46,52], 2D [39,45,48,49] and 3D [47].

2.3 Long-range and nearest-neighbor interactions

We also consider a system including both LR and NN interaction terms. This interplay of one long-range and two short-range interactions is especially interesting, as the NN interactions suppress a simultaneous high occupancy on even and odd sites. The LR interactions, on the contrary, might support the forming of such a structure in certain areas of the parameter space.

3 Methods/simulation

For this work, the ground state properties of the systems were investigated using the Variational Monte-Carlo (VMC) method [63,64]. Generally speaking, VMC is a form of QMC, in which the ground state of a quantum system is approximated by variational methods. The starting point is an appropriate trial wave function $|\Psi_T\rangle$ depending on a set of optimization parameters. The optimal values of these parameters, and thereby the optimized wave function, are found by minimizing the total energy of the system. Occurring integrals are evaluated via QMC. A detailed description of the VMC approach can be found in reference [54]. We present a short summary of this in the appendix. The optimizations suggested by reference [65] have been included in our algorithm.

3.1 Phases and order parameters

In the standard BHM, only kinetic and local potential energies compete, resulting in two phases denoted superfluid and Mott insulator. These are balanced in terms of occupancy of even and odd sites. The introduction of the additional NN and LR interaction terms in the extended models gives rise to additional phases. An MI-like phase is expected to appear, in which bosons are localized but an imbalance in the occupancy of even and odd sites exists. This phase is denoted density wave (DW) phase

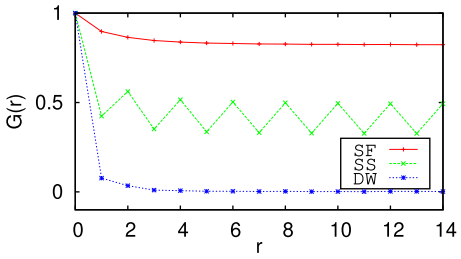

Fig. 1. Phase coherence correlation function in different phases of a LR interacting system with $L^2 = 196$ sites and $\rho = 1$ at a fixed ratio $U_l/U_s = 0.7$. The SF phase was measured at $U_s = 5$, SS at $U_s = 8$ and DW at $U_s = 15$.

and does not appear for arbitrary fillings, but only at integer or half-integer fillings. Furthermore, a superfluid-like phase is introduced, in which bosons are delocalized and an imbalance in the occupation number of even and odd sites occurs. This phase is called the supersolid phase and might appear for arbitrary densities ρ. As there are now four phases to consider, at least two order parameters are necessary to in distinct them.

It is useful to consider the phase coherence correlation function

$$G(\boldsymbol{R}) = \frac{1}{2L^2}\sum_{\boldsymbol{r}}\langle \hat{b}^\dagger_{\boldsymbol{r}}\hat{b}_{\boldsymbol{r}+\boldsymbol{R}} + \text{H.c.}\rangle, \tag{2}$$

where $\boldsymbol{R}$ is the distance between two sites and the brackets $\langle\cdots\rangle = \langle\Psi|\ldots|\Psi\rangle$ denote the mean value of an observable in the system state $|\Psi\rangle$. As an example, we show the phase coherence functions in different phases, taken from cuts through the phase diagram of a system with LR interactions, in Figure 1. One observes that in addition to indicating boson delocalization $G(r)$ displays in the SS phase an even-odd modulation similar to the density-density correlation function. The number of particles of the system with a wave vector $\boldsymbol{k}$ is given by the Fourier transform $n(\boldsymbol{k})$ of the phase coherence correlation function,

$$n(\boldsymbol{k}) = \frac{1}{L^2}\sum_{\boldsymbol{R}} e^{i\boldsymbol{k}\cdot\boldsymbol{R}} G(\boldsymbol{R}), \tag{3}$$

whose value for $\boldsymbol{k} = \boldsymbol{0}$ is the condensate fraction, which is the fraction of bosons occupying the superfluid ground state.

In analogy to the phase coherence correlation function used to distinguish localized and delocalized phases, the density-density correlation function $C(\boldsymbol{R})$ is introduced,

$$C(\boldsymbol{R}) = \frac{1}{L^2}\sum_{\boldsymbol{r}}\langle \hat{n}_{\boldsymbol{r}}\hat{n}_{\boldsymbol{r}+\boldsymbol{R}}\rangle, \tag{4}$$

whose Fourier transform $S(\boldsymbol{k})$ is the structure factor

$$S(\boldsymbol{k}) = \frac{1}{L^2}\sum_{\boldsymbol{R}} e^{i\boldsymbol{k}\cdot\boldsymbol{R}} C(\boldsymbol{R}). \tag{5}$$

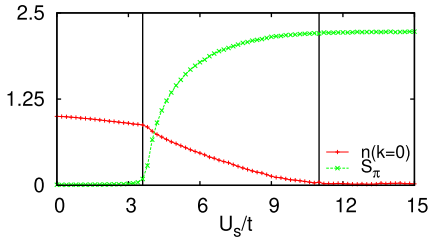

Fig. 2. Continuous transition in 2D for a LR system with $L^2 = 196$ sites and $\rho = 1.5$ for a fixed ratio $U_l/U_s = 0.8$ from SF ($n(\boldsymbol{k} = \boldsymbol{0}) \neq 0$, $S_\pi = 0$) over SS ($n(\boldsymbol{k} = \boldsymbol{0}) \neq 0$, $S_\pi \neq 0$) to DW phase ($n(\boldsymbol{k} = \boldsymbol{0}) = 0$, $S_\pi \neq 0$).

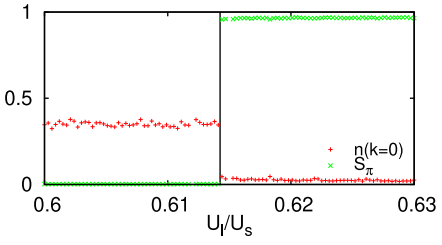

Fig. 3. First order transition in a LR system with $L^2 = 196$ for a fixed $U_s = 15$ in 2D at $\rho = 1$ from SF ($n(\boldsymbol{k} = \boldsymbol{0}) \neq 0$, $S_\pi = 0$) to DW phase($n(\boldsymbol{k} = \boldsymbol{0}) = 0$, $S_\pi \neq 0$).

The value of $S(\pi) = S_\pi$ is particularly useful because the exponential in the Fourier transform takes the value 1 when two sites of distance $\boldsymbol{R}$ have equal parity and -1 when the sites have different parity. Thus we expect S_π to be zero in the MI and SF phases, and non-zero in the DW and SS phases. With these order parameters, we can distinguish all four occurring phases. The actual value of S_π is necessary to evaluate the quality of the DW phase at higher densities because different imbalances between even and odd sites might be possible. In order to distinguish between first and second order phase transitions, we have to consider whether the order parameters change continuously or not. Figure 2 shows an example of the evolution of structure factor and condensate fraction during two second-order phase transitions in a system with LR interactions. Figure 3 shows an example for a first order phase transition from SF to DW in the same system. Both order parameters $n(\boldsymbol{k} = \boldsymbol{0})$ and S_π have a discontinuity at the point where the first order phase transition takes place.

As stated before, an important aspect to keep in mind is the possibility of metastable states. In this paper, we only consider ground state properties. But we are treating systems in which multiple interactions with similar strengths compete. Especially near phase transitions, we have to ensure the proper equilibration of the system in order to reach the true ground state of each parameter configuration. VMC allows us to compute kinetic and potential energies. In case several local minima are present, we can run simulations for different initial states to detect the ground state. An example of this can be seen in Figure 4, where we can read the phase transition between two DW phases from the crossing of the energies.

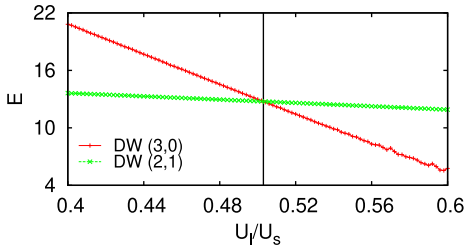

Fig. 4. Comparison of the ground state energy at different initial states DW (3,0) and DW (2,1) for a system with $L^2 = 256$ sites, $U_s = 30$ and $\rho = 1.5$. A first-order phase transition occurs where curves cross.

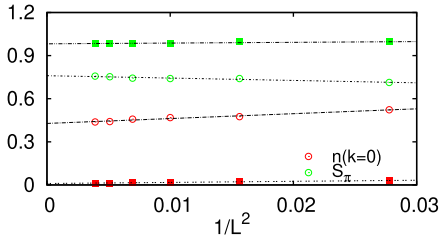

Fig. 5. Thermodynamic limit extrapolation of structure factor S_π and condensate fraction $n(\boldsymbol{k} = \boldsymbol{0})$ at $t = 1$, $U_l/U_s = 0.8$ in the CDW ($U_s = 11$, filled squares) and SS ($U_s = 7$, empty circles) phases. Black lines are linear fit.

Since all our simulations operate at finite system sizes, it is possible that we observe pseudo-order in the system once the correlation length ξ approaches the size of the system L. Hence the critical points of phase transitions become depended on the system size. Figure 5 shows the extrapolation of $n(\boldsymbol{k} = \boldsymbol{0})$ and S_π in the thermodynamic limit in SS and DW phases. This extrapolation shows that a system-size of $L^2 = 196$ sites is sufficient to get a good estimate of the thermodynamic limit.

4 Results

All simulations treat systems in 2D and the tunneling-strength was fixed at $t = 1$ to set the energy scale. Simulations were generally executed for $L \times L = 196$ square lattices, as we showed before that this is a suitable choice. Phase diagrams are presented either in the $(U_s/t, U_{IA}/t)$- or $(U_s/t, U_{IA}/U_s)$-plane (with $U_{IA} \in \{U_l, U_{nn}\}$) and were acquired by considering cuts through the parameter space in with respect to the change in the order parameters, as illustrated in Figures 2, 3 and 4. To determine the exact locations of the phase transitions, finite-size scaling was done, which is elaborated in the next section.

If not stated otherwise, the simulations have been performed with 500 optimization-iterations and 1 million Monte-Carlo steps before the final measurements.

4.1 Long-range interactions

The first phase diagram is presented in the $(U_s/t, U_l/t)$-plane and covers a system with particle density $\rho = 1$. The tunneling t is fixed to $t = 1$ to set the scale, but U_s and U_l are still in similar range. The full diagram is shown in Figure 6a. The two insulating phases, MI and DW, as well as the SF and a stable SS were identified and there are five different direct transitions between phases. At low U_s/t, the system is never insulating, but there is a second-order phase transition from SF to SS (red line in Fig. 6a) when the LR tuning U_l is large enough. The SS phases in Figures 6a, 6b and 6c extend down to infinitesimally small $U_s > 0$. Increasing the on-site repulsion, a transition from SF to MI takes place (teal line). Using finite-size scaling, we find that this second order transition takes place at $U_s/t = 18.4$. This agrees well with the results by other groups using QMC simulations, where the transition is determined to take place at $U_s/t = 17$ [49]. The corresponding phase diagram is reprinted in Figure 7. Taking the inverse of our value $t/U_s = 0.054$, it is also in fair agreement with the critical value for the standard BHM in 2D $(t/U_s)_{BH} = 0.05974$ [18]. This is to be expected, as the LR interaction term does not contribute to the ground-state energy of both the SF- and the MI-phase. For this reason, the transition in the LR interacting system is not shifted in comparison to the standard BHM and independent of U_l.

The transitions from SF to DW (blue line) and MI to DW (purple line) are first-order transitions, while there is a continuous phase transition between SS and DW (green line).

All four phases are present and take in large areas. It should be noted that there is a (roughly) diagonal line throughout the diagram, which separates the phases with no spatial imbalance (SF, MI) from the ones with a non-zero structure factor (SS, DW). The slope of this line gives us the critical ratio between U_s and U_l at which the dominant force changes. A fit of this is illustrated in Figure 9a, in which the slope was determined to be $m_l = 0.55(\pm 0.01)$. This is slightly higher than the theoretical value $m = 0.5$, because the LR interaction in the Hamiltonian becomes dominant above a ratio of $U_l/U_s = 0.5$. The DW phase in this diagram has the structure $(2, 0)$, Figure 3 shows the evolution of condensate fraction and structure factor in a cut at $U_s/t = 15$. It shows a first order phase transition from SF to DW, as there is a discontinuity in both these parameters. We are especially interested in the competition between the LR interaction and the short-range on-site potential, so it helps to rescale the plot of the phase diagram in Figure 6a to the $(U_s/t, U_l/U_s)$-plane. This is depicted in Figure 6d. Transition lines between phases have the same color code as in the previous phase diagram. For low U_l/U_s, only SF and MI phases exist. At higher ratios, SS and DW phases appear. The phase diagram obtained by QMC from reference [49] is reprinted in Figure 7. Moving on to phase diagrams for different densities, we keep the system size fixed but vary the number of bosons. Figure 8a exhibits the corresponding diagram for $\rho = 0.5$. At half-integer densities, in our case a system of $L^2 = 196$ sites with $N = 98$ bosons, the formation of an MI is impossible. Consequently, the phase diagram depicts only three different phases: SF, DW and a small region which seems to be SS. However, QMC studies have shown that for $\rho = 0.5$ the SS phase is unstable and in fact a region of phase separation between SF and SS [49].

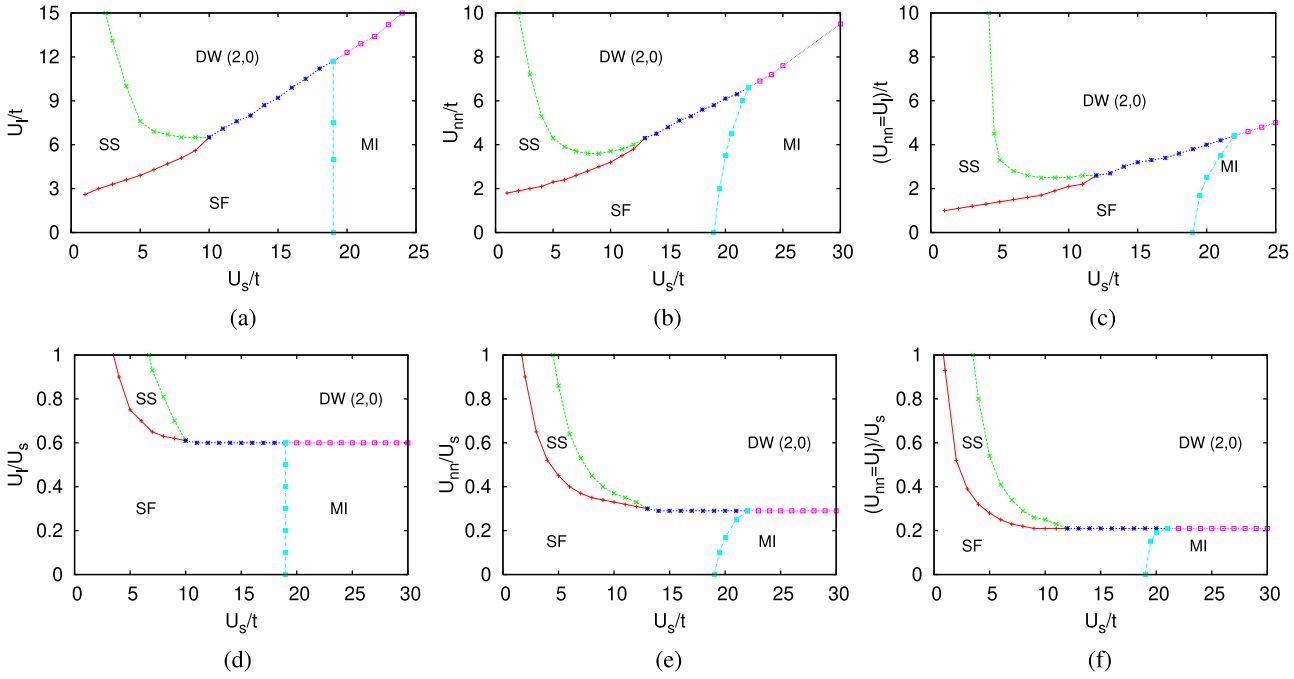

Fig. 6. Ground state phase diagrams at $\rho = 1$ for systems with (a) LR interactions; (b) NN interactions; (c) LR and NN interactions equally strong. The observed phases are superfluid (SF), supersolid (SS), Mott insulator (MI) and density-wave (DW). (d)–(f) depict rescaled phase diagrams for better comparability of on- and off-site interactions.

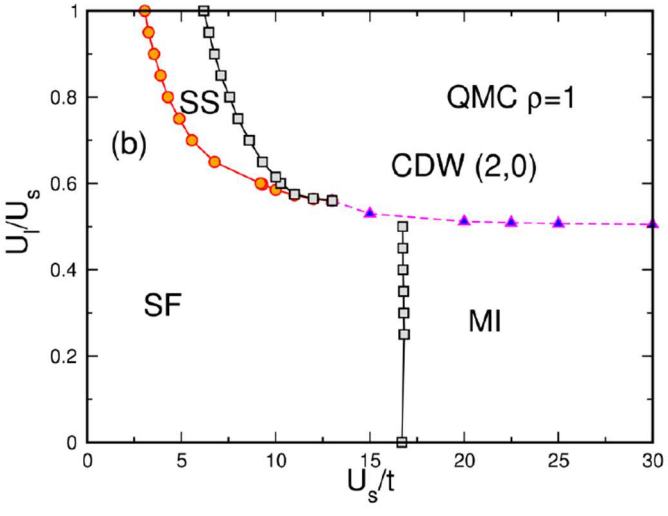

Fig. 7. Phase diagram of the LR system from Figure 6d obtained with QMC methods. Originally published in reference [49]. (Reprinted with permission, @ 2017 by the American Physical Society.)

In contrast, the SS phase is stable for $\rho = 1$, $\rho = 1.5$ and $\rho = 2$.

For larger values of U_s/t, the phase-separated region disappears and there is a direct first-order transition between SF and DW. The DW has the structure $(1, 0)$ this time. A critical point where all three regions meet can be found at $U_s/t = 18$. A system with $\rho = 1.5$ delivers a rich phase diagram, with interestingly shaped phase transition lines and two different DW phases. It can be seen in Figure 8b. Note the absence of a direct transition between SF and DW. In the area covered by our diagram, these phases are always separated by a thin but stable SS phase. The width of this intermediate area varies with the ratio U_l/U_s. Most interesting about this diagram is, however, the coexistence of two varieties of the DW phase. Tuning U_l/U_s between roughly 0.4 and 0.5 in combination with high on-site repulsion results in an insulating DW (2,1) phase, with a low imbalance between even and odd sites. Increasing the ratio of U_l/U_s results in the formation of a DW (3,0) phase, associated with a higher imbalance in occupancy between sites of different parities. Both DW phases are separated by a first-order transition and distinguished by their ground state energy as shown in Figure 4. As a consequence, the SS domain contains two visible lobes split by this first order transition. The structure factor continuously converges to 9/4 in the upper lobe while approaching the DW domain, whereas it converges to 1/4 in the lower one. All diagrams obtained via the VMC algorithm presented here can be compared to those presented in [49] by QMC and mean-field methods. Actually, the VMC is closer to the QMC than to the MF. Especially the SF to DW transition in the $\rho = 1$ domain and the qualitative shape of the SF domain in the $\rho = 1.5$ are well described by the variational description contrary to the mean-field method.

The phase diagram for $\rho = 2$ is presented in Figure 8c and it is very similar to the one for $\rho = 1$ (seen in Fig. 6d), regarding the shape of the phases. SF is larger here, as the transition between SF and MI phases shifted to $U_s/t = 32$, which corresponds to $t/U_s = 0.0313$. This is close to the value for the corresponding transition in the standard BHM, which was determined to be $t/U_s = 0.035$ [23]. For similar reasons as in the $\rho = 1$-diagram, this was

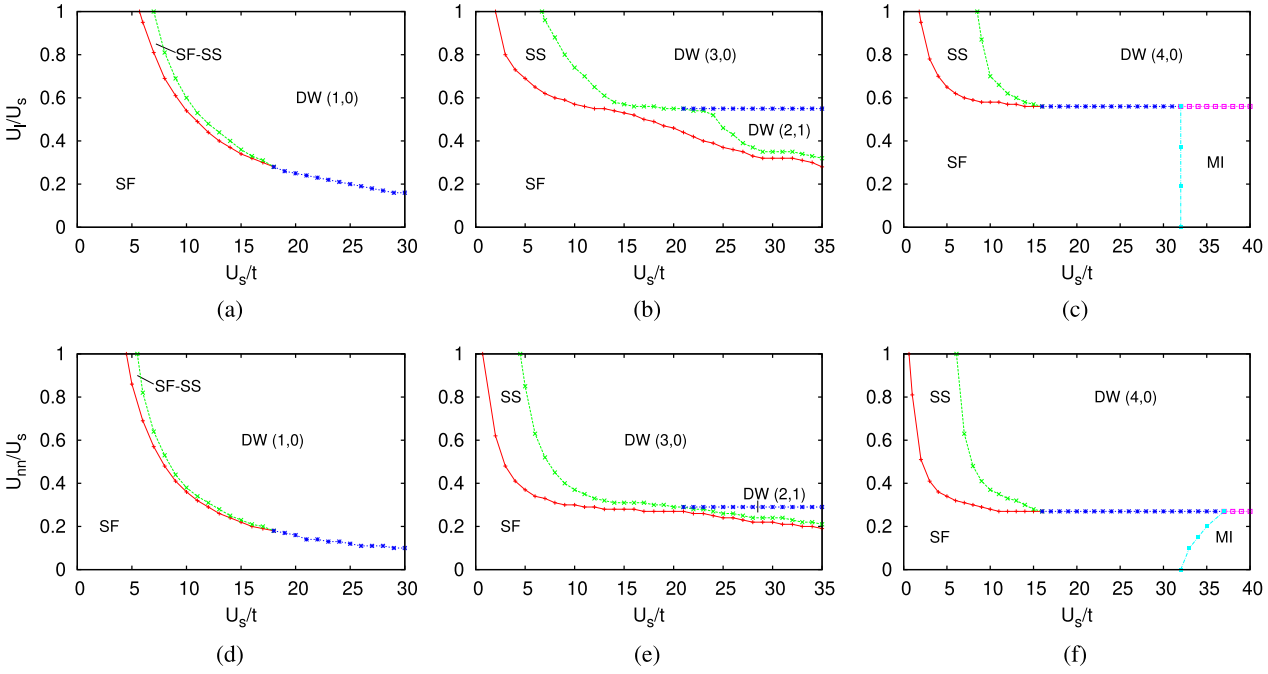

Fig. 8. Top row: phase diagrams of systems with LR interactions at (a) $\rho = 0.5$, (b) $\rho = 1.5$, (c) $\rho = 2$. Bottom row: phase diagrams of systems with NN interactions at (d) $\rho = 0.5$, (e) $\rho = 1.5$, (f) $\rho = 2$. The MI phase only appears at integer densities. Two different stable DW phases exist at $\rho = 1.5$.

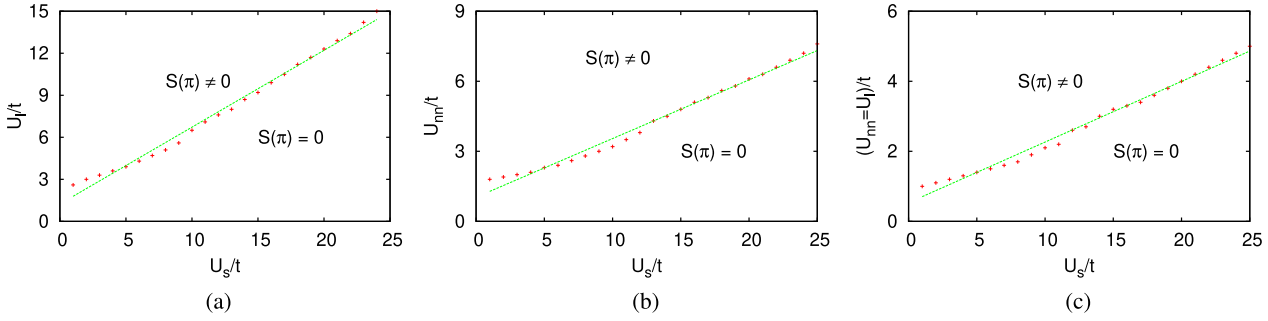

Fig. 9. (a) Linear fit of the transition line that separates the section of phase diagram without imbalance ($S(\pi) = 0$) and the section with imbalance. The fit reveals a slope of $m_l = 0.55$. In theory, we would expect the transition to be at $m = 0.5$; (b) linear fit of the transition line that separates the section of phase diagram without imbalance ($S(\pi) = 0$) and the section with imbalance. The fit reveals a slope of $m_{nn} = 0.252$. In theory, we would expect the transition to be at $m_t = 0.25$; (c) linear fit of the transition-line between phases with vanishing structure factor and $S_\pi > 0$. The slope was measured as $m = 0.175$.

to be expected: LR interactions do not affect the ground-state energies of the involved phases. In the $\rho = 2$-case, the DW phase forms the occupation structure $(4, 0)$, obviously a consequence of the increased density. There is no DW $(3, 1)$ area in the ground state, however. Unlike in the $\rho = 1.5$-diagram, there is only one occupation pattern in the DW phase. Compared to $\rho = 1$, the tricritical point between SF, SS and DW shifted from $U_s/t = 10$ to $U_s/t = 16$.

4.2 Nearest-neighbor interactions

The phase diagram of the system with nearest-neighbor interactions at $\rho = 1$, shown in Figure 6b, is similar to the equivalent diagram in the LR case (Fig. 6a). While the overall structure is very much alike, the transition between SF and MI phases depends on U_{nn} in the NN system. This behavior can be explained by considering the effect of the NN interaction on the SF and the MI phases. The NN term significantly increases the ground-state energies, and the contribution becomes maximal in the MI phase. Therefore, a higher U_s/t is necessary to enter this phase and the transition, in this case, depends on the strength of U_{nn}. The transition-line to the phases with spatial imbalance, however, has a different slope. We determined it once again by a linear fit, seen in Figure 9b. Comparing the result $m_{nn} = 0.252$ to the one of the LR system $m_l = 0.55$ (Fig. 9a), we note that it is smaller by a factor 2, which is what we would expect, considering the $t = 0$ limit of both systems.

Comparing the rescaled $\rho = 1$ plots for NN (Fig. 6e) and LR interacting systems (Fig. 6d) approves the observations regarding the imbalanced phases.

As mentioned in the LR section, the $\rho = 0.5$-case (Fig. 8d) is special because it contains a region of phase separation between SF and SS. Like in the LR model, there is no stable SS phase. At densities $\rho = 1$, $\rho = 1.5$ and $\rho = 2$, the SS is stable in the system with NN interactions. The main difference to the LR phase-diagram for this density (Fig. 8d) is the shift in U_{nn}/U_s-direction. The imbalanced phases begin to form at lower U_{nn}/U_s-ratios than in the LR case. On the other hand, the ratio where all regions meet is the same as in the LR case, located at $U_s/t = 18$. Moving on to $\rho = 1.5$, Figure 8c shows an interesting NN phase-diagram, particularly with regard to the equivalent LR diagram (Fig. 8b). Again, the featured phases are SF, SS, DW$(2,1)$ and DW$(3,0)$. Within the range of parameters covered by the diagram, there is no direct transition from SF to DW phases. An intermediate, stable SS area is present, like in the LR phase-diagram. While there is a first-order transition from DW$(2,1)$ to DW$(3,0)$, all other transitions are continuous. Comparing NN and LR phase diagrams, we note the tricritical point between SS, DW$(2,1)$ and DW$(3,0)$ takes place at a ratio of $U_s/t = 21$ in both cases, but the overall shape of the phases is considerably different. With NN interactions, the SS-phase is much smaller for higher U_s/t and the DW$(2,1)$-phase is less pronounced in general. The LR interactions, however, feature a large stable DW$(2,1)$ in its ground state phase-diagram. Figure 8f shows the phase diagram at density $\rho = 2$. It resembles the long-range diagram (Fig. 8c), critical points at which three phases meet occur at $U_s/t = 16$ (SF, SS, DW) and $U_s/t = 33$ (SF, MI, DW). No DW$(3,1)$-phase was observed in the ground-state, only DW$(4,0)$. The fact that phase diagrams for systems with LR and NN interactions are so similar goes in line with former considerations, predicting NN and LR systems to behave equally in the mean-field limit [46]. However, the SF-MI-transition is different in both cases, because of different contributions of NN interactions to the ground-state energy of both phases, while LR interactions do not affect them.

4.3 Long-range and nearest-neighbor interactions

In this section, we continue our investigation by considering systems featuring both NN and LR interactions. Together with the tunneling term and the on-site repulsion, there is now a competition between one long-range force term and multiple short-range interactions. Although NN and LR interactions promote the same order in the system, it will be interesting to know where the phase-transitions will be located. LR and NN interactions are chosen to be equally strong at $\rho = 1$. The resulting phase diagram is presented in Figure 6c. The phase diagram strongly resembles those with only LR (Fig. 6a) and only NN (Fig. 6b) interactions. While the transition-line from SF to MI has a similar shape as in the NN model, which makes sense as the LR interaction does not affect both phases, the critical point where SF, SS and DW phases meet takes place at $U_s/t = 12$ and thereby lies between the equivalent values for LR ($U_s/t = 10$) and NN interactions ($U_s/t = 13$). As in the sections above, we additionally present a linear fit to determine the critical ratio between the phases with and without spatial imbalance (Fig. 9c). The slope corresponding to the critical ratio is determined as $(U_l = U_{nn})/U_s = 0.175$. In comparison to LR ($U_l/U_s \approx 0.5$) and NN ($U_{nn}/U_s \approx 0.25$) only, this value is lower. This is to be expected since there are now two similarly strong interactions that drive the system towards a state with structure factor $S_\pi > 0$. The SF-MI-transition behaves just like in the NN only case, which is to be expected, regarding the fact that the LR interactions do not affect both phases. When both interactions are tuned simultaneously by the same factor, the combination of both works like one effective, single interaction. In comparison to the individual interactions, the transition between SF and MI remains unaffected. But transition-lines involving phases with $S_\pi > 0$ are altered.

4.4 Phase-transitions and finite-size scaling

Every phase transition goes along with the breaking of at least one symmetry. The inherent symmetries in our Hamiltonians are the $U(1)$-symmetry associated with particle number conservation and the $\mathbb{Z}_2$-symmetry associated with the nearest-neighbor and long-range interactions. A non-vanishing structure factor S_π signifies the breaking of the $\mathbb{Z}_2$ translational symmetry, while a non-zero condensate fraction $n(\mathbf{k})$ indicates a broken $U(1)$ symmetry. If the change in order-parameter is discontinuous, it is associated with a first order phase transition. If it is continuous, the phase transition is second order [66]. The second-order phase transitions are expected to belong to the 3D Ising and 3D XY universality classes [67] respectively. In the following, we use finite-size scaling to locate the continuous phase-transition points accurately and to determine the critical exponents.

Between the four different phases we observed so far, there are five direct transitions. First order phase transitions take place between MI and DW and between SF and DW phases. $\mathbb{Z}_2$ symmetry is broken in the former when the spatial modulation arises. Both symmetries are broken in the latter, as we have shown in Figure 3. MI to SF, SS to DW and SF to SS are second-order phase transitions with a broken $U(1)$ symmetry due to the occurring superfluidity in the first two, and a broken $\mathbb{Z}_2$ symmetry in the SF-SS transition, where S_π becomes non-zero.

Before beginning with the finite-size scaling analysis of the second-order phase transitions of the extended models, we look into the limit $U_l = U_{nn} = 0$, the standard BHM. The enclosed graph in Figure 10a shows the SF to MI transition in this case for varying system-sizes. The corresponding order parameter is the condensate fraction, which is plotted as a function of U_s. For the finite-size scaling, we use the critical exponents of the 3D XY universality class, $\beta = 0.348$ and $\nu = 0.671$. The point where the curves cross indicates the critical point, we measure $(U_s/t)_c = 18.4$ or $(t/U_s)_c = 0.054$. As already stated above, this value is close to the literature value $(t/U_s)_{BH} = 0.05974$ [18]. A finite size scaling plot is shown in Figure 10a, where $\delta = (U_s - (U_s)_c)/(U_s)_c$ represents the normalized distance to the critical value $(U_s)_c$. The data collapse is good and confirms the crossing at $(U_s/t)_c = 18.4$.

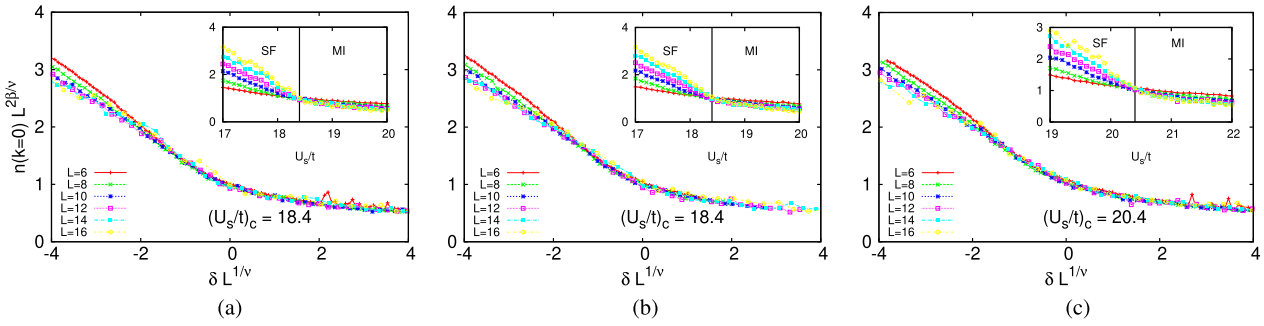

Fig. 10. Comparison of the SF-MI-transition in the (a) standard BHM ($U_l = U_{nn} = 0$), (b) BHM with LR ($U_l/U_s = 0.1$, $U_{nn} = 0$), (c) BHM with NN interactions ($U_{nn}/U_s = 0.2$, $U_l = 0$), rescaled using the 3D XY scaling exponents $\beta = 0.348$ and $\nu = 0.671$ to produce a data-collapse.

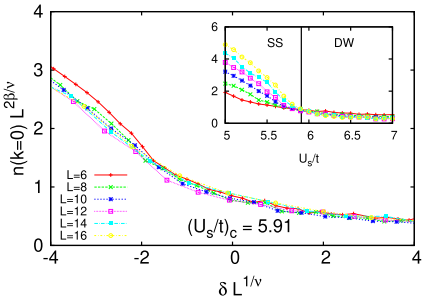

Fig. 11. SS-DW-transition in the NN interacting system at $U_{nn}/U_s = 0.7$, rescaled using the 3D XY scaling exponents $\beta = 0.348$ and $\nu = 0.671$.

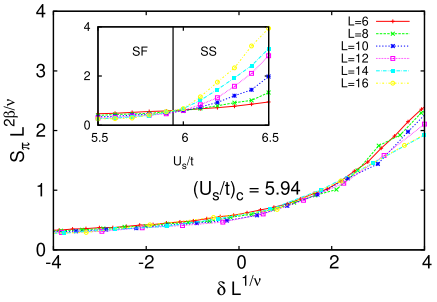

Fig. 12. SF-SS-transition, indicated by a change of the structure factor S_π, in a system with long-range interactions at $U_l/U_s = 0.7$. The 3D Ising exponents $\beta = 0.326$ and $\nu = 0.630$ are used as the transition should belong to this universality class. The phase transition was determined by the crossing of the unscaled curves in the small picture.

Figures 10b and 10c show the same transition in the model with LR and NN interactions. The critical point is shifted in the NN case because of the effect of the off-site interactions on the ground state energies, as explained above. Considering the quality of the crossings and data collapse in Figures 10a, 10b and 10c, the VMC seems capable of predicting the correct universality class of the SF-MI transition.

To illustrate the SS-DW phase transition, where there is also a $U(1)$ symmetry breaking, we choose the NN model as an example and fix $U_{nn}/U_s = 0.7$. Using the 3D XY exponents,the critical point is found at $(U_s/t)_c = 5.91$. A finite-size scaling plot and a data collapse can be seen in Figure 11. To investigate the SF to SS phase transition, we tune U_l (compare Fig. 6d). The corresponding order parameter is the structure factor S_π. The critical exponents of the 3D Ising universality class are $\beta = 0.326$ and $\nu = 0.630$. The inset of Figure 12 shows the crossing of the S_π curves at fixed ratio $U_l/U_s = 0.7$ and the main graph shows the finite-size scaling plot. The phase transition takes place at $(U_s/t)_c = 5.94$.

5 Discussion and conclusion

The mean-field theory predicts the Bose-Hubbard model with long-range and nearest-neighbor interactions to have the same phase-diagram [46]. In our results, however, they differ quantitatively as well as qualitatively. The difference is most remarkable in the transition between SF and MI phases. It takes place at a fixed ratio of U_s/t in the system with long-range interactions, but the critical value for U_s/t depends on U_{nn} in the presence of nearest-neighbor interactions.

Although all variational states in our calculations are translationally invariant, our results are closer to the exact QMC methods than to mean-field theory.

This work showed that the Variational Monte-Carlo method is capable of providing reliable results for bosonic systems with long- and short-range interactions. The phase diagrams for the long-range interactions are in good agreement with former results by other groups. Our data corroborate the numerical results already obtained and it also supports the experimental results [42]. This shows that our Ansatz-wavefunction and the variational parameters, consisting of Jastrow- and many-body-factors, provide a good description of the Bose-Hubbard model with infinity-range interactions. Starting from this, we also investigated a Bose-Hubbard model with nearest-neighbor interactions. We observed the phase diagrams to be fairly similar in shape, but with differences in the size of phases and in the transition between SF and MI phases in particular.

We want to thank Giovanna Morigi and Rebecca Kraus for useful discussions. We also thank Nicolò Defenu, Laurent de

Forges de Parny and Johannes Sicks the useful discussions about phase transitions and critical phenomena and Thierry Fredrich for his tireless technical support.

Author contribution statement

All the authors contributed equally to the paper.

Appendix A

A.1 Variational Monte-Carlo method

Variational Monte-Carlo is a form of quantum Monte-Carlo, in which the ground state of a quantum system is approximated by variational methods. Starting point is an appropriate trial wave function $|\Psi_T\rangle$ which depends on a set of optimization parameters. The optimal values of these parameters, and thereby the optimized wave function, are found by minimizing the total energy of the system. Occuring integrals are evaluated via QMC. A more detailed description of the VMC approach can be found in reference [54]. Also, the optimizations suggested by reference [65] have been included.

We start with the trial wave function

$$|\Psi_T\rangle = \exp\left(\frac{1}{2}\sum_{i,j} v_{i,j}\hat{n}_i\hat{n}_j + g_{MB}\sum_i \hat{\xi}_{h-d,i}\right)|\Psi_0\rangle, \tag{A.1}$$

where $|\Psi_0\rangle = \left(\sum_i \hat{b}_i^\dagger\right)^N |0\rangle$ is the ground state of a non-interacting ($U_s = U_l = U_{nn} = 0$) system of N bosons. The first term in the exponential of (A.1) is named Jastrow factor, while the second one is called many-body operator [68]. Parameters $v_{i,j}$ and g_{MB} are to be optimized. The Jastrow factor allows to control density-density correlations between sites, and to reduce the number of parameters. Here, we use periodic boundary conditions and regard the Hamiltonian as translationally invariant, so the parameters $v_{i,j} = v(|\boldsymbol{R}_i - \boldsymbol{R}_j|)$ only depend on the distance between sites i and j. In the second term, $\sum_i \hat{\xi}_{h-d,i}$ counts the number of isolated holons and doublons in the system, where holons are empty sites and doublons are doubly occupied sites.

$$\hat{\xi}_{h-d,i} = \hat{h}_i \prod_{\boldsymbol{\delta}}(1 - \hat{d}_{i+\boldsymbol{\delta}}) + \hat{d}_i \prod_{\boldsymbol{\delta}}(1 - \hat{h}_{i+\boldsymbol{\delta}}). \tag{A.2}$$

The summation over $\boldsymbol{\delta}$ connects the site i with its nearest neighbors, $\hat{h}_i$ is 1 if the site is empty and 0 otherwise, $\hat{d}_i$ is 1 if the site is doubly occupied and 0 otherwise. The many-body operator controls short-range interactions [68]. It might control wether the holon-doublon pairs are able to unbind and propagate freely in the system or not, via the parameter g_{MB}, which has proven to increase accuracy for bosonic systems in the insulating phase in 2D and 3D [54]. While this is a good choice for simulations with $\rho = 1$, the parameter should be improved upon at higher densities. We modified the variational wave-function in order to investigate systems with density $\rho = 2$. The holon-doublon interaction described in (A.2) was changed to a singlon-triplon interaction by replacing $\hat{\xi}_{h-d,i}$ by $\hat{\xi}_{s-t,i}$ with

$$\hat{\xi}_{s-t,i} = \hat{s}_i \prod_{\boldsymbol{\delta}}(1 - \hat{t}_{i+\boldsymbol{\delta}}) + \hat{t}_i \prod_{\boldsymbol{\delta}}(1 - \hat{s}_{i+\boldsymbol{\delta}}). \tag{A.3}$$

The summation over $\boldsymbol{\delta}$ still connects site i with its nearest neighbors, but this time $\hat{s}_i$ is 1 if the site contains a single boson (i.e. a singlon) and 0 otherwise, $\hat{t}_i$ is 1 if the site is triply occupied (i.e. a triplon) and 0 otherwise. This interaction is more suited to the $\rho = 2$, as it describes the deviation from the average occupation. Starting from the most symmetrical case where all sites contain exactly ρ, singlon-triplon pairs are created by a boson hoping to one of its nearest neighbors. Analogously, holon-doublon pairs are created by fluctuations in the $\rho = 1$ system. The phase diagrams seen in Figures 8c and 8f were constructed with the help of this modification.

Other works showed that $|\Psi_T\rangle$ is a decent trial state for the standard Bose-Hubbard Hamiltonian [54], which contains only on-site interactions, and it also has been discussed that the Jastrow factor is able to describe long-range interactions [55]. Consequently, it is suitable to simulate the model with short- as well as long-range interactions. Since even and odd sites play equivalent roles in the system, the assumption $v_{i,j} = v(|\boldsymbol{R}_i - \boldsymbol{R}_j|)$ still holds, and thus strongly reduces the number of parameters. As we will see in the following section, the order parameters we use behave in the same way for pairs of sites i, j and i', j' with $R = |\boldsymbol{R}_i - \boldsymbol{R}_j| = |\boldsymbol{R}_{i'} - \boldsymbol{R}_{j'}|$. Therefore, the $v_{i,j}$ are well suited to reproduce the symmetries in the Hamiltonians, including the long-range interaction.

As we are interested in the ground-state properties of the system, it is our goal to optimize $|\Psi_T\rangle$ in a way that its corresponding energy E_T is as close to the true ground-state energy of $\hat{\mathcal{H}}$ as possible. In order to optimize the variational parameters, we start with the system in occupation number representation. The system then undergoes a Monte-Carlo algorithm, in which the dynamics of the Hamiltonian are stochastically calculated via Metropolis-like sampling. This means that bosons are randomly proposed to change their site and the proposal is accepted or rejected depending on the change in energetic properties. These local changes in energy, that follow the properties of the Hamiltonion, are then used to compute the variational parameters, which is described in detail in [65].

We propose a trial wave function $|\Psi_T(\boldsymbol{\alpha})\rangle$, depending on a set of p parameters α_k, $k = 1, \ldots, p$ and impose explicit form of $|\Psi_T(\boldsymbol{\alpha})\rangle$ such that whenever parameters α_k are specified, all components of the trial wave function in number basis $\{|n_1, n_2, \ldots\rangle\}$ are known. In our case, the parameters α_k are the Jastrow-factors $v_{i,j}$ and the many-body term g_{MB}.

Basis for the Monte-Carlo sampling is now the variational theorem, which states that the true ground-state E_0 of a system described by the Hamiltonian $\hat{\mathcal{H}}$ is always lower or equal to the normalized expectation-value $E_T(\boldsymbol{\alpha})$

in respect to $\hat{\mathcal{H}}$:

$$E_0 \leq E_T(\boldsymbol{\alpha}) = \frac{\langle\Psi_T(\boldsymbol{\alpha})|\hat{\mathcal{H}}|\Psi_T(\boldsymbol{\alpha})\rangle}{\langle\Psi_T(\boldsymbol{\alpha})|\Psi_T(\boldsymbol{\alpha})\rangle}.$$

This means that by optimizing $|\Psi_T(\boldsymbol{\alpha})\rangle$, our approximation $E_T(\boldsymbol{\alpha})$ will only approach E_0 but not undercut it. Inserting closure relations and rewriting the energy as

$$E_T(\boldsymbol{\alpha}) = \frac{\sum_n |\langle n|\Psi_T(\boldsymbol{\alpha})\rangle|^2 E_L(n,\boldsymbol{\alpha})}{\sum_n |\langle n|\Psi_T(\boldsymbol{\alpha})\rangle|^2}$$

with

$$E_L(n,\boldsymbol{\alpha}) = \frac{\langle n|\hat{\mathcal{H}}|\Psi_T(\boldsymbol{\alpha})\rangle}{\langle n|\Psi_T(\boldsymbol{\alpha})\rangle},$$

is very useful. This is where MC sampling comes into play. If random vectors $|n\rangle$ are picked from the number basis, distributed according to the probability distribution

$$\rho(n) = \frac{|\langle n|\Psi_T(\boldsymbol{\alpha})\rangle|^2}{\sum_{n'} |\langle n'|\Psi_T(\boldsymbol{\alpha})\rangle|^2},$$

an estimate of $E_T(\boldsymbol{\alpha})$ is obtained by averaging $E_L(n,\boldsymbol{\alpha})$ over M stochastically generated configurations $|n\rangle$:

$$E_T(\boldsymbol{\alpha}) = \frac{1}{M}\sum_{i=1}^{M} E_L(n_i,\boldsymbol{\alpha}).$$

Now we have a good estimate for the energy of the trial wave-function with the set of parameters $\boldsymbol{\alpha}$. In order to optimize the wave-function by finding a better set of parameters $\boldsymbol{\alpha}' = \boldsymbol{\alpha} + \boldsymbol{\gamma}$, an operator $\mathcal{O}_k$ for each parameter α_k is defined:

$$\mathcal{O}_k(n) = \frac{\partial_{\alpha_k}\Psi_T(\alpha,n)}{\Psi_T(\alpha,n)}.$$

The updated wave-function $|\Psi_T(\boldsymbol{\alpha}+\boldsymbol{\gamma})\rangle$ with the new set of parameters $\boldsymbol{\alpha}' = \boldsymbol{\alpha} + \boldsymbol{\gamma}$ in second order Taylor approximation can be expressed by means of the operators $\mathcal{O}_k$:

$$|\Psi_T(\boldsymbol{\alpha}+\boldsymbol{\gamma})\rangle \approx \left[1 + \sum_k \gamma_k(\mathcal{O}_k - \langle\mathcal{O}_k\rangle) + \frac{\beta}{2}\sum_{k,k'}\gamma_k\gamma_{k'}(\mathcal{O}_k - \langle\mathcal{O}_k\rangle)(\mathcal{O}_{k'} - \langle\mathcal{O}_{k'}\rangle)\right]|\Psi_T(\boldsymbol{\alpha})\rangle$$

where $\beta = 1$ in the Taylor-expansion, but is used here as a parameter to optimize the iteration scheme [65].

To review if the new set of parameters is an improvement, the change in the mean value of the energy between $|\Psi_T(\boldsymbol{\alpha})\rangle$ and $|\Psi_T(\boldsymbol{\alpha}+\boldsymbol{\gamma})\rangle$ has to be checked:

$$\Delta E = -\sum_k \gamma_k f_k + \frac{1}{2}\sum_{k,k'}\gamma_k\gamma_{k'}[S_h^{k,k'} + (1+\beta)G^{k,k'}].$$

All quantities can be calculated with the help of local energy $E_L(n,\boldsymbol{\alpha})$ from the Monte-Carlo sampling:

$$\begin{aligned} f_k &= -\partial_{\alpha_k}E_T(\boldsymbol{\alpha}) = -2\left[\langle E_L\mathcal{O}_k\rangle\langle E_L\rangle\langle\mathcal{O}_k\rangle\right], \\ S_h^{k,k'} &= \langle[\mathcal{O}_k,[\hat{\mathscr{H}},\mathcal{O}_{k'}]]\rangle \\ &= \langle\partial_{\alpha_k}E_L\mathcal{O}_{k'}\rangle - \langle\partial_{\alpha_k}E_L\rangle\langle\mathcal{O}_{k'}\rangle, \\ G^{k,k'} &= 2\langle\langle E_L\rangle(\mathcal{O}_k - \langle\mathcal{O}_k\rangle)(\mathcal{O}_{k'} - \langle\mathcal{O}_{k'}\rangle)\rangle. \end{aligned}$$

This is how the parameters are optimized. Clearly, the minimum energy is obtained for $\boldsymbol{\gamma} = B^{-1}\boldsymbol{f}$ with $B = S_h + (1+\beta)G$. The initial state of the MC algorithm becomes a valuable tool in critical regions, as the system may not reach the true ground state if we choose a wrong starting configuration.

References

1. M.P. Fisher, P.B. Weichman, G. Grinstein, D.S. Fisher, Phys. Rev. B **40**, 546 (1989)
2. V.A. Kashurnikov, B.V. Svistunov, Phys. Rev. B **53**, 11776 (1996)
3. G.G. Batrouni, R.T. Scalettar, G.T. Zimanyi, Phys. Rev. Lett. **65**, 1765 (1990)
4. G.G. Batrouni, R.T. Scalettar, Phys. Rev. B **46**, 9051 (1992)
5. W. Krauth, N. Trivedi, Europhys. Lett. **14**, 627 (1991)
6. W. Krauth, N. Trivedi, D. Ceperley, Phys. Rev. Lett. **67**, 2307 (1991)
7. D.M. Ceperley, Rev. Mod. Phys. **67**, 279 (1995)
8. N. Prokof'ev, B. Svistunov, I. Tupitsyn, Phys. Lett. A **238**, 253 (1998)
9. N. Prokof'ev, B. Svistunov, Phys. Rev. Lett. **87**, 160601 (2001)
10. N. Prokof'ev, B. Svistunov, Phys. Rev. Lett. **92**, 015703 (2004)
11. N. Kawashima, K. Harada, J. Phys. Soc. Jpn. **73**, 1379 (2004)
12. M. Boninsegni, N.V. Prokof'ev, B.V. Svistunov, Phys. Rev. E **74**, 036701 (2006)
13. V.G. Rousseau, Phys. Rev. E **77**, 056705 (2008)
14. V.G. Rousseau, Phys. Rev. E **78**, 056707 (2008)
15. F. Alet, E.S. Sørensen, Phys. Rev. B **70**, 024513 (2004)
16. M. Köhl, H. Moritz, T. Stöferle, C. Schori, T. Esslinger, J. Low Temp. Phys. **138**, 635 (2005)
17. B. Capogrosso-Sansone, N.V. Prokof'ev, B.V. Svistunov, Phys. Rev. B **75**, 134302 (2007)
18. B. Capogrosso-Sansone, S.G. Söyler, N. Prokof'ev, B. Svistunov, Phys. Rev. A **77**, 015602 (2008)
19. T. Ohgoe, T. Suzuki, N. Kawashima, Phys. Rev. B **86**, 054520 (2012)
20. E. Duchon, N. Trivedi, Ann. Phys. **525**, L35 (2013)
21. S.R. White, Phys. Rev. Lett. **69**, 2863 (1992)
22. W. Krauth, M. Caffarel, J.P. Bouchaud, Phys. Rev. B **45**, 3137 (1992)
23. N. Elstner, H. Monien, Phys. Rev. B **59**, 12184 (1999)
24. T.D. Kühner, H. Monien, Phys. Rev. B **58**, R14741 (1998)
25. T.D. Kühner, S.R. White, H. Monien, Phys. Rev. B **61**, 12474 (2000)
26. T. Kimura, Phys. Rev. A **84**, 063630 (2011)
27. K. Kawaki, Y. Kuno, I. Ichinose, Phys. Rev. B **95**, 195101 (2017)

28. D. Jaksch, C. Bruder, J.I. Cirac, C.W. Gardiner, P. Zoller, Phys. Rev. Lett. **81**, 3108 (1998)
29. M. Greiner, O. Mandel, T. Esslinger, T.W. Hänsch, I. Bloch, Nature **415**, 39 (2002)
30. I. Bloch, J. Dalibard, W. Zwerger, Rev. Mod. Phys. **80**, 885 (2008)
31. H. Ritsch, P. Domokos, F. Brennecke, T. Esslinger, Rev. Mod. Phys. **85**, 553 (2013)
32. O. Dutta, M. Gajda, P. Hauke, M. Lewenstein, D.S. Lühmann, B.A. Malomed, T. Sowiński, J. Zakrzewski, Rep. Prog. Phys **78**, 066001 (2015)
33. G.G. Batrouni, R.T. Scalettar, G.T. Zimanyi, A.P. Kampf, Phys. Rev. Lett. **74**, 2527 (1995)
34. M. Boninsegni, N.V. Prokof'ev, Rev. Mod. Phys. **84**, 759 (2012)
35. P. Sengupta, L.P. Pryadko, F. Alet, M. Troyer, G. Schmid, Phys. Rev. Lett. **94**, 207202 (2005)
36. G.G. Batrouni, F. Hébert, R.T. Scalettar, Phys. Rev. Lett. **97**, 087209 (2006)
37. K.W. Mahmud, E.N. Duchon, Y. Kato, N. Kawashima, R.T. Scalettar, N. Trivedi, Phys. Rev. B **84**, 054302 (2011)
38. G.G. Batrouni, R.T. Scalettar, V.G. Rousseau, B. Grémaud, Phys. Rev. Lett. **110**, 265303 (2013)
39. D. Rossini, R. Fazio, New J. Phys **14**, 065012 (2012)
40. B. Grémaud, G.G. Batrouni, Phys. Rev. B **93**, 035108 (2016)
41. A.E. Niederle, H. Rieger, New J. Phys **15**, 075029 (2013)
42. R. Landig, L. Hruby, N. Dogra, M. Landini, R. Mottl, T. Donner, T. Esslinger, Nature **532**, 476 (2016)
43. T. Keller, S.B. Jäger, G. Morigi, J. Stat. Mech. Theory Exp. **2017**, 064002 (2017)
44. Y. Li, L. He, W. Hofstetter, Phys. Rev. A **87**, 051604 (2013)
45. A.E. Niederle, G. Morigi, H. Rieger, Phys. Rev. A **94**, 033607 (2016)
46. N. Dogra, F. Brennecke, S.D. Huber, T. Donner, Phys. Rev. A **94**, 023632 (2016)
47. Y. Chen, Z. Yu, H. Zhai, Phys. Rev. A **93**, 041601 (2016)
48. B. Sundar, E.J. Mueller, Phys. Rev. A **94**, 033631 (2016)
49. T. Flottat, L.d.F. de Parny, F. Hébert, V.G. Rousseau, G.G. Batrouni, Phys. Rev. B **95**, 144501 (2017)
50. H. Habibian, A. Winter, S. Paganelli, H. Rieger, G. Morigi, Phys. Rev. Lett. **110**, 075304 (2013)
51. J. Panas, A. Kauch, K. Byczuk, Phys. Rev. B **95**, 115105 (2017)
52. B. Blaß, H. Rieger, G.m.H. Roósz, F. Iglói, Phys. Rev. Lett. **121**, 095301 (2018)
53. F. Iglói, B. Blaß, G.m.H. Roósz, H. Rieger, Phys. Rev. B **98**, 184415 (2018)
54. M. Capello, F. Becca, M. Fabrizio, S. Sorella, E. Tosatti, Phys. Rev. Lett. **94**, 026406 (2005)
55. L. Cevolani, G. Carleo, L. Sanchez-Palencia, Phys. Rev. A **92**, 041603 (2015)
56. A. van Otterlo, K.H. Wagenblast, R. Baltin, C. Bruder, R. Fazio, G. Schön, Phys. Rev. B **52**, 16176 (1995)
57. K. Yamamoto, S. Todo, S. Miyashita, Phys. Rev. B **79**, 094503 (2009)
58. B. Xi, F. Ye, W. Chen, F. Zhang, G. Su, Phys. Rev. B **84**, 054512 (2011)
59. D.L. Kovrizhin, G.V. Pai, S. Sinha, EPL (Europhysics Letters) **72**, 162 (2005)
60. M. Iskin, Phys. Rev. A **83**, 051606 (2011)
61. S. Rist, C. Menotti, G. Morigi, Phys. Rev. A **81**, 013404 (2010)
62. J.S. Douglas, K. Burnett, Phys. Rev. A **84**, 033637 (2011)
63. W.L. McMillan, Phys. Rev. **138**, A442 (1965)
64. D. Ceperley, G.V. Chester, M.H. Kalos, Phys. Rev. B **16**, 3081 (1977)
65. S. Sorella, Phys. Rev. B **71**, 241103 (2005)
66. J.M. Kosterlitz, D.J. Thouless, J. Phys. C **6**, 1181 (1973)
67. M. Campostrini, M. Hasenbusch, A. Pelissetto, P. Rossi, E. Vicari, Phys. Rev. B **63**, 214503 (2001)
68. H. Yokoyama, H. Shiba, J. Phys. Soc. Jpn. **59**, 3669 (1990)